Study of Residual Stresses in Additively Manufactured Ti-6Al-4V by Neutron Diffraction Measurements

DAVID GLOAGUEN, BAPTISTE GIRAULT, BRUNO COURANT, PIERRE-ANTOINE DUBOS, MARIE-JOSÉ MOYA, FRANÇOIS EDY, and JOANA REBELO KORNMEIER

Neutron diffraction is a powerful non-destructive volumetric evaluation method for the analysis of the internal stress state in components processed by laser powder bed fusion (LPBF). High cooling rates and heterogeneous distribution of temperature during additive manufacturing lead to large residual stress fields. Residual stresses developed during the building process have unquestionably an important influence on the mechanical performance and potentially lead to delamination from the support structures, shape distortion but also crack formation. In the present work, neutron measurements have been carried out on cube-shaped samples prepared by LPBF from a Ti-6Al-4V powder bed. A series of miscellaneous positions (center, edge, and corner) over three different depths (close substrate, middle, and close surface) have been analyzed by neutron diffraction so as to systematically characterize the full stress tensor. The influence of shear stresses and second-order residual stresses on the stress tensor analysis is also discussed in this work.

I. INTRODUCTION

ADDITIVE manufacturing (AM) techniques of metallic parts are expanding rapidly due to the technologic stake they represent: lightening of structure, complex architecture structure, or reduced post-treatment processes.[1] Laser Powder Bed Fusion (LPBF) has a tremendous potential in AM methods because it enables to produce fully dense parts with desired inner structure and surface morphology.[2] LPBF technology can be used with various metallic powder materials such as Ti-6Al-4V,[3,4] iron-based materials,[5] and stainless steel.[6] Ti-6Al-4V is an alloy characterized by a combination of high strength, low-density, and good corrosion resistance. Due to its biocompatibility, Ti-6Al-4V is ideal for medical applications and is also one of the main alloys used for high-temperature aerospace applications as a result of its high strength to weight ratio and good corrosion properties. Over the last decade, LPBF machines have become more and more popular in industrial settings which have led to extensive research regarding the potential use of LPBF for high added value functional Ti-6Al-4V parts production.

The high-temperature gradient, as a result of the locally concentrated energy input, can lead to property gradients arising from the different interdependent physical phenomena (metallurgical, thermal, mechanical, and fluid mechanics aspects) occurring during this highly non-equilibrium process.[6] As a consequence, the LPBF process can result in residual stress gradients, likely large, and hence, crack formation and part deformations which have a significant effect on the macroscopic mechanical performance.[7,8] Therefore, it is an important issue to understand the development of residual stresses in LPBF processed components.

Internal stresses develop in built components due to the high cooling rates, the thermal gradients and the volumetric changes arising during phase transformations occurring during the process.[9] Additionally, multiple process parameters have a significant influence on the development of internal stresses. It has been notably shown that baseplate nature, power bed pre-heating, powder characteristics, laser power, scanning speed, scanning strategy, number and thickness of

DAVID GLOAGUEN, BAPTISTE GIRAULT, BRUNO COURANT, PIERRE-ANTOINE DUBOS, and MARIE-JOSÉ MOYA are with the Université de Nantes, Institut de Recherche en Génie Civil et Mécanique, UMR CNRS 6183), 58, rue Michel Ange - BP 420, 44606 Saint-Nazaire Cedex, France. Contact e-mail: david.gloaguen@univ-nantes.fr. FRANÇOIS EDY is with the IRT Jules Verne (French Institute in Research and Technology in Advanced Manufacturing), Bouguenais, France, JOANA REBELO KORNMEIER is with the Heinz Maier-Leibnitz Zentrum (MLZ), Technische Universität München, Garching, Germany.
Manuscript submitted June 10, 2019.
Article published online November 11, 2019.

the successive layers, and the geometry of the part for Ti-6Al-4V have a significant impact on the residual stress set up.[8,10] Most of the process parameters (typically scan speed and laser power) cannot be varied independently, as a fully dense part always needs to be obtained. It is not necessarily easy to distinguish the influence of individual process parameters on the internal stress generated during the process. In this complex multi-parameter process, the investigation of the relationship set between LPBF parameters values and residual stress formation is still necessary.

Although residual stresses are deeply studied for analogous processes such as multi-pass welding, there are still too few experimental or/and numerical studies concerning the residual stresses in components processed by LPBF.[10]

Nevertheless, producing as-built parts of near full density and having mechanical properties similar to those met for conventionally manufactured bulk materials (like casting or forging) remains one of the most important goals of the AM community. The development of an in-depth expertise of stress setup for AM materials is thus required to achieve such a goal, especially if certification protocols need to be developed for AM components commissioning. A major element of this process study involves the development of accurate and reliable material property databases such as residual stress.

In most cases, residual macroscopic stresses are determined through a large variety of methods which can be divided into two categories: destructive (contour method,[11] hole drilling,[12] crack-compliance[13]) or non-destructive (e.g., X-ray and neutron diffraction[6,14,15] methods). Each of those has drawbacks and benefits and varies in terms of probed volume, accuracy or destruction level which can lead to a marked dispersion around results reported in the literature. The most commonly used as non-destructive methods are X-ray (XRD) and neutron diffraction (ND), which permit, respectively, close surface (i.e., a few tens of microns at best for conventional X-ray equipment) and volumetric residual stress analysis in metallic materials.[16] Within this framework, ND is particularly relevant since neutrons have a large penetration depth in most metallic alloys[6,17,18] up to cm length scale, enabling non-destructive mapping of stress components through the full depth of an AM part.

Nevertheless, two major drawbacks exist as regard to ND method for residual stress analysis. The first one is the low acquisition rates of ND coupled with a long beam time acquisition. The second is the extremely limited access to neutron sources. Furthermore, in order to provide the full stress tensor defined by six independent components, although strain measurement in six independent directions is mathematically sufficient, it is more suitable to overdetermine the system by performing measurements in at least 12 directions to reduce the related uncertainty.[16] In order to reduce the long measurement time due to the low acquisition rates of ND, one strong assumption is commonly made so that the number of measurement directions is reduced. It consists in assuming that the principal stress directions are known and can be inferred from the sample geometry.[6,16,19] Strain measurements can then be limited to these three (orthogonal) directions to resolve the principal stress components σ_1, σ_2, σ_3. For single track LPBF specimens, it seems to be reasonable to assume that the principal stress, σ_1, is along the scan track; σ_2, lies in the perpendicular direction and σ_3, lies in the direction perpendicular to the baseplate (i.e., parallel to the plan formed by σ_1 and σ_2).[6,15,20] For more complex laser exposure strategies, this assumption is even less self-evident and needs to be used carefully. If the shear stress components are not equal to zero, the principal stress values determined with this assumption are simply wrong. As far as we know, the determination of the full stress tensor has never been performed in Ti-6Al-4V parts obtained by LPBF, whatever the laser exposure strategy used.

In the present work, ND measurements were carried out on cube-shaped samples ($10 \times 10 \times 10$ mm^3) built by LPBF from a Ti-6Al-4V powder bed. A series of miscellaneous positions (center, edge, and corner) over three different depths (close substrate, middle, and close surface) have been analyzed. In order to obtain a substantial data set for strain analysis, 3 {hk.l} reflections and 10 measurement directions for each reflection are probed at each analyzed position, so as to systematically characterize the full strain tensor. Despite 6 strain directions would have been sufficient to determine all the tensor components, data acquisition has been five-fold increased enabling to check the reliability of the data and assess the significance of shear stresses. In most of the studies, stress analysis by XRD or ND is only performed with a single {hk.l} reflection. The importance of second-order (or intergranular) stresses is never quantified or even considered. A specific study is carried out in this paper to investigate the importance of these stresses in samples prepared by LPBF.

II. EXPERIMENTAL

A. Specimen Preparation

The parts used for this study were designed and built at the IRT Jules Verne (French Institute in Research and Technology in Advanced Manufacturing, Bouguenais—France). Cube-shaped specimens ($10 \times 10 \times 10$ mm^3) were produced using a SLM Solutions 280HL machine. They were built from a Ti-6Al-4V powder (grade 23 ELI) with the following chemical composition: Ti—balance, Al—6 pct, V—4 pct, Fe ≤ 0.25 pct, O ≤ 0.13 pct, H ≤ 0.012 pct, C ≤ 0.08 pct and N ≤ 0.05 pct (weight percent). The metallurgical characterization has been presented in a previous study where more details concerning the analysis can be found.[21] Briefly, a SEM analysis of the powder has shown a mostly spherical grain morphology with minimal satellites or smaller particles bonded to larger particles. An analysis of the powder achieved by a laser scattering technique has showed a particle size distribution spread between 20 and 63 μm with a median size of d_{50} = 43 μm. The LPBF process was optimized to

obtain an acceptable level of final part density. The final parameters used to manufacture the specimens were: 30 μm-thick powder layers, a laser power of 175 W, a beam diameter of 80 μm, a scanning velocity of 775 mm s^{-1} and a hatch spacing of 120 μm. The build plate was made of the same Ti-6Al-4V alloy as the powder and was heated to a constant temperature of 200 °C during the process. Concerning the scanning strategy, the starting point of the building process is located on the edge of the part to be built. Each layer is then built through a back and forth laser path with a rotation of 90 deg of the main laser path-vector between each layer. SEM observations have revealed that a porosity density level of approximately 0.01 deg is obtained. Optical microscopy analysis showed the formation of fully columnar structures along the LPBF building direction which is in accordance with the literature.

B. Stress Analysis by Neutron Diffraction

First and foremost, it is worth to recall the stress analysis principles by diffraction and the different associated assumptions.[16] The measured mean lattice strain $\langle \varepsilon(hk.l, \varphi, \psi) \rangle V_d$ over the diffracting volume V_d, for grains having the scattering vector Q (defined by inclination and azimuth angles, respectively ψ and φ, as introduced in Figure 1) perpendicular to the {hk.l} planes, can be calculated from the measured lattice spacing $\langle d(hk.l, \varphi, \psi) \rangle V_d$ and a reference one $d_0(hk.l)$ using the following expression based on the true (rational) strain definition[22]:

$$\langle \varepsilon(hk.l, \varphi, \psi) \rangle V_d = \ln \left(\frac{\langle d(hk.l, \varphi, \psi) \rangle V_d}{d_0(hk.l)} \right) \quad [1]$$

where $d_0(hk.l)$ is the strain-free lattice parameter related to the considered {hk.l} reflection, $\langle \ \rangle V_d$ denotes an averaging over diffracting grains for the considered {hk.l} plane family.

The lattice strain along the scattering vector can be calculated once 2θ angle has been determined from measured diffraction peak using:

$$\langle \varepsilon(hk.l, \varphi, \psi) \rangle V_d = \ln \left(\frac{\sin \theta_0(hk.l)}{\sin \theta(hk.l, \varphi, \psi)} \right) \quad [2]$$

where θ_0 is the Bragg angle regarding the stress-free material. The most appropriate solution to determine this stress-free parameter in LPBF specimens consists in digging out this value from a stress relaxed mini-cube ($2 \times 2 \times 2$ mm^3), cut from twin specimens at the exact position of the stress measurement (incorporating thus the metallurgical state of the measuring points). The mini-cubes are then beam centered thanks to direct beam absorption measurements and a theodolite device. Diffraction patterns are recorded while successively rotating around z and x axes of the part coordinate system (x, y, z) (Figure 1). This results in an in-plane ((x, y); φ-scan from 0 to 360 deg at ψ = 0 deg) and out of plane (y,z) (ψ-scans from 0 to 90 deg at φ = 0 deg) averaging of the lattice spacing.[6,23]

In order to resolve the macroscopic stress tensor σ, diffraction patterns have to be performed along various directions (defined by ψ and φ angles). $\langle \varepsilon(hk.l, \varphi, \psi) \rangle V_d$ values for those directions can thereafter be used to calculate the stress tensor using the following relationship:

$$\langle \varepsilon(hk.l, \varphi, \psi) \rangle V_d = F_{ij}(hk.l, \varphi, \psi)\sigma_{ij} \quad [3]$$

$F_{ij}(hk.l, \varphi, \psi)$ are the diffraction stress factors for the considered {hk.l} reflection.[24] These factors can be calculated from material single-crystal elastic data and the Orientation Distribution Function (ODF), thanks to an appropriate scale transition model. For
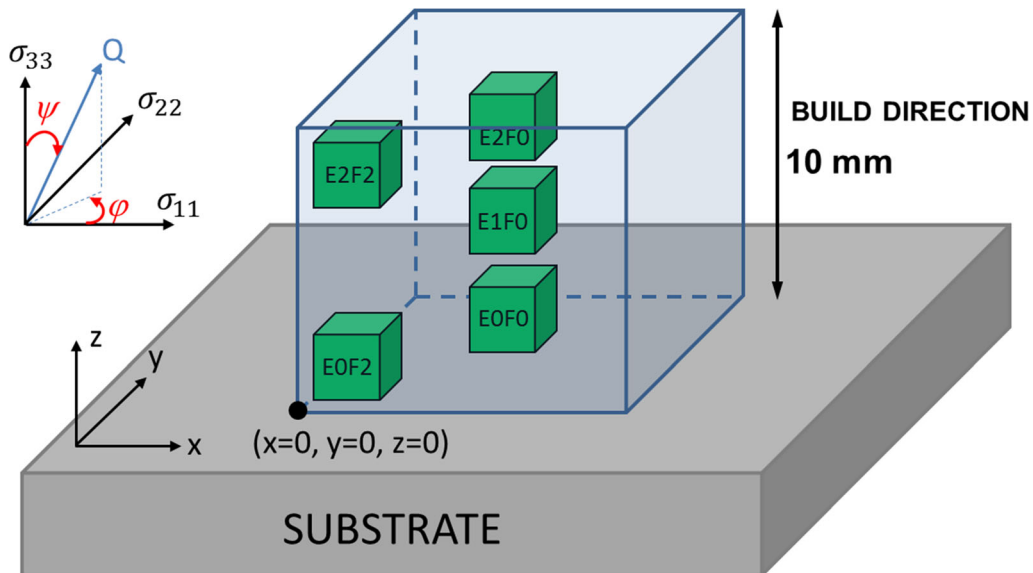

Fig. 1—Schematic of the sample with measurement positions (in green) taken in the analysis. Note the coordinate system (x, y, z) where x and y directions are parallel to the baseplate and the z direction is the part building direction (Color figure online).

macroscopically elastically anisotropic samples, it is important to specify that this relation remains valid. In Eq. [3], the second-order stresses (or intergranular stresses) are however neglected. The deviations of grain stresses from macroscopic stresses are then considered as exclusively resulting from elastic anisotropy. The deviations due to the anisotropy of the thermal expansion coefficients, plastic anisotropy, or heterogeneity of phase transformation are not explicitly taken into account.[25]

For quasi-isotropic materials having no preferential crystallographic orientation (i.e., elastically anisotropic grains in a randomly distributed crystallographic orientation sample), the correlation between the lattice strains obtained in measuring directions (φ, ψ) and the full stress tensor is simply given by:

$$
\begin{aligned}
&\langle \varepsilon(hk.l, \varphi, \psi) \rangle V_d \\
&= \frac{1}{2} S_2(hk.l) \left[\sigma_{11} \cos^2 \varphi + \sigma_{12} \sin^2 \varphi + \sigma_{22} \sin^2 \varphi \right] \sin^2 \psi \\
&+ \frac{1}{2} S_2(hk.l) [\sigma_{13} \cos \varphi \sin 2\psi + \sigma_{23} \sin \varphi \sin 2\psi \\
&+ \sigma_{33} \cos^2 \psi] + S_1(hk.l)[\sigma_{11} + \sigma_{22} + \sigma_{33}]
\end{aligned}
$$

[4]

$\frac{1}{2} S_2(hk.l)$ and $S_1(hk.l)$ are the well-known X-ray Elastic Constants (XEC).[16,26] They depend on the measured {hk.l} reflection and take into account the elastic anisotropy of the grain.

If the principal stress coordinate system is known, only lattice strain measurements along these three orthogonal directions are required to determine the full stress tensor, which is diagonal in this case. The relation between the principal stress components σ_i and the principal strain components ε_j is then given by:

$$
\begin{aligned}
\sigma i &= \frac{\left(2S_1(hk.l) + \frac{1}{2} S_2(hk.l) \right)}{\frac{1}{2} S_2(hk.l) \left(3S_1(hk.l) + \frac{1}{2} S_2(hk.l) \right)} \varepsilon_i \\
&- \frac{(S_1(hk.l)))}{\frac{1}{2} S_2(hk.l) \left(3S_1(hk.l) + \frac{1}{2} S_2(hk.l) \right)} \sum_j \varepsilon_j \\
&\quad j = 1, 2, 3 \quad j \neq i
\end{aligned}
$$

[5]

For a polycrystal composed of elastically isotropic grains, the residual principal stresses are simply calculated from the measured strains by the following relationship:

$$
\sigma_i = \frac{E(1 - v)}{(1 + v)(1 - 2v)} \varepsilon_i + \frac{Ev}{(1 + v)(1 - 2v)} \sum_j \varepsilon_j \\
j = 1, 2, 3 \quad j \neq i
$$

[6]

where E and v are, respectively, the Young's modulus and Poisson's ratio of the polycrystalline aggregate.

Experiments have been performed at STRESS-SPEC beamline (Heinz Maier-Leibnitz Zentrum—MLZ)[27] where one cube-shaped ($10 \times 10 \times 10$ mm³) base-plate-supported sample has been analyzed. A monochromatic incident neutron wavelength of 1.55 Å has been chosen for the measurements. A χ goniometric assembly with a Position Sensitive Detector (³He-PSD) was used.[28] 3 reflections were studied: {10.3} at 2θ = 71.9 deg, {11.2} at 2θ = 77.9 deg and {20.1} at 2θ = 79.2 deg. The recording time for each ND measurement of a {hk.l} peak took around 60 min. Peak positions were determined by fitting the experimental data with a Pseudo-Voigt function and a polynomial background.

A series of miscellaneous positions (center, edge, and corner) over 3 different depths (close substrate, middle, and close surface) has been probed by ND (Figure 1). Gauge volume has been chosen as a compromise between acceptable measurement time scale and position resolution in volume (i.e., $2 \times 2 \times 2$ mm³). Gauge position coordinates have integrated geometrical concerns ensuring the gauge to remain within the sample volume no matter the selected measurement direction, even for rim analyses. Five different gauge positions have been achieved (Figure 1) to analyze the residual stress distribution throughout the depth of the Ti alloy cube with a practicable testing time.

In order to obtain a consequent data set for strain analyses, 10 (φ,ψ) directions per diffraction peak have been probed on each of the five strain gauge positions: (0, 0 deg), (0, 30 deg), (0, 60 deg), (0, 90 deg), (45, 30 deg), (45, 60 deg), (45, 90 deg), (90, 30 deg), (90, 60 deg), (90, 90 deg). Figure 2 shows an example of ND patterns where diffraction intensities are plotted as function of the measured Bragg angle 2θ for the E1F0 measurement position. The differences in intensities of the different diffraction peaks for the (φ, ψ) directions point to the presence of a crystallographic texture in the LPBF part.

The XEC have been calculated from single-crystal elastic constants ($c_{11} = c_{22} = 162.4$ GPa, $c_{33} = 180.7$ GPa, $c_{12} = 92$ GPa, $c_{13} = 69$ GPa, and $c_{44} = 46.7$ GPa[29]) using an elastic-self consistent model.[30] For the calculation, we assume that the effect of crystallographic texture is low because the individual crystallites of the polycrystal are characterized by a low elastic
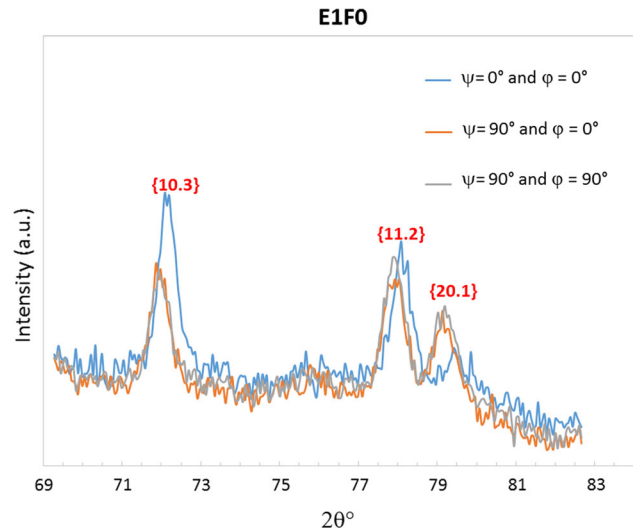

Fig. 2—Neutron diffraction patterns of the Ti-6Al-4V sample for different (φ, ψ) directions for the E1F0 measurement position. The diffraction peaks used in the study are also given.

anisotropy ($\frac{c_{11}+c_{12}-c_{33}}{c_{13}} = 1.07$, $\frac{c_{66}}{c_{44}} = 0.75$, $\frac{c_{11}+c_{12}+c_{33}}{4c_{44}} = 1.07$ for titanium[31]). For the stress calculations, the quasi-isotropic assumption is used. The calculated XEC, $\frac{1}{2}S_2(hk.l)$ and $S_1(hk.l)$, necessary for the stress calculation, are:

$$\frac{1}{2}S_2(10.3) = 10.87 \times 10^{-6} \text{ MPa}^{-1}, \ S_1(10.3)$$
$$= -2.58 \times 10^{-6} \text{ MPa}^{-1};$$

$$\frac{1}{2}S_2(11.2) = 11.72 \times 10^{-6} \text{ MPa}^{-1}, \ S_1(11.2)$$
$$= -2.88 \times 10^{-6} \text{ MPa}^{-1};$$

$$\frac{1}{2}S_2(20.1) = 11.95 \times 10^{-6} \text{ MPa}^{-1}, \ S_1(20.1)$$
$$= -2.96 \times 10^{-6} \text{ MPa}^{-1}.$$

The full stress tensor is calculated according to the Eq. [4] for each measurement position.

III. RESULTS AND DISCUSSION

A. *Origin of the Residual Stresses in the LPBF Process*

As a first step, it may be useful to recall the physical origins of the residual stresses being built in this manufacturing process. LPBF is characterized by a complex thermal cycle. It is defined by several phenomena: high heating and cooling rates, melt-back inducing the simultaneous melting of the upper material layer (powder bed) and re-melting of underlying previously solidified layers. The fast heating-cooling thermal cycles of LPBF associated with volumetric changes, caused by both phase transformations and temperature gradients, generate large residual stresses within LPBF parts.

Mercelis and Kruth[9] proposed a useful two-stage mechanism to explain how residual stresses occur during the LPBF process: the temperature gradient mechanism (TGM) and the cool-down stage. The TGM enables describing the stress generation in a single melt track while the cool-down mechanism depicts the behavior of an entirely melted powder layer. In the TGM model, due to the fast warming of the top surface by the laser beam, the material expands thermally. This thermal expansion of the heated top layer is restricted by the colder underlying material. This phenomenon generates compressive stresses in the heat-affected zone. Meanwhile, the material yield strength is reduced due to the temperature rise. If the expansion is sufficiently significant, the compressive stress in the constrained solid material exceeds the material yield strength and the top layer is then plastically compressed. During the cooling, as a result of thermal contraction, shrinkage of the top layers tends to occur. The underlying material limits this deformation and elastic tensile strains are thus introduced in the plastically deformed area which is balanced by a compressive zone below.[32] In the framework of the cool-down model, the melted top layer initially has a higher temperature than the underlying one. When the melt zone has cooled and solidified, the added top layer shrinks owing to thermal contraction. This deformation is inhibited by the surrounding colder material. Therefore, tensile stresses appear in the newly solidified upper layer and they are balanced by compressive stresses in the underlying layers. Although these two models clearly describe the major mechanisms involved in the residual stress generation during LPBF, the stress field is naturally much more complex since the number of layers, the heat source path pattern, and the heat transfer are tremendously intricate.[33]

B. *Evolution of Stress Components of the Full Stress Tensor*

Figures 3(a) and (b) show the evolution of stress components of the full stress tensor at 3 building heights ($z = 1.73, 5.00, 8.27$ mm) in the core sample *i.e.*, central column F0 ($x = y = 5$ mm), coordinates matching the center of each probed volume. Let us first focus on the development of the σ_{33} component for the central column F0 (Figure 3(a)). Large negative stress ($\sigma_{33} = -487 \pm 41$ MPa) at low z values (near the baseplate) decreasing with higher z values (the minimum stress is found at $z = 8.27$ mm: $\sigma_{33} = -135 \pm 20$ MPa) is observed in measurements. At this point, it must be reminded that the gauge volume ($2 \times 2 \times 2$ mm^3) probed in neutron experiments is large as compared to the thickness of the melted layers. The sample, built with 30 μm layer thickness, results in 67 layers per probed volume so it means that the stresses are averaged over a large number of layers. Thus, it must be kept in mind that the results obtained by ND indicate an average stress value and not an extremum value.

The stress value obtained at $z = 8.27$ mm is the mean stress obtained for a depth varying from 6.54 up to 10 mm and not the close-surface stress value. The residual stress increases rapidly toward low compressive values as the top surface is approached. The normal stress could thus even reach positive values at the subsurface. The heat transfer is actually weak along the building direction, leading to a high-temperature gradient, bringing up tensile σ_{33} stress in the upper section and compressive stress in the bottom section *i.e.*, in the nearest region of the baseplate. The stresses along the building direction correspond to the process described above by the cool-down mechanism. Lower longitudinal (σ_{11}) and transversal (σ_{22}) stress level were present along the sample height which turned into tension ($\sigma_{11} = 43 \pm 19$ MPa) in the upper region. The laser scanning strategy, for which the laser path direction is alternated between each layer [0/90 deg], tends to provide a homogeneous stress field in the *x*-*y* plane (Figure 4).

According to the residual stress analysis presented by Ali *et al.*[34] increasing powder bed pre-heating temperatures results in a lowering of residual stress due to a reduction in temperature gradients during the LPBF process. On the other hand, components that remain attached to the baseplate contain stress levels close to the material yield strength value without pre-heating.[35]
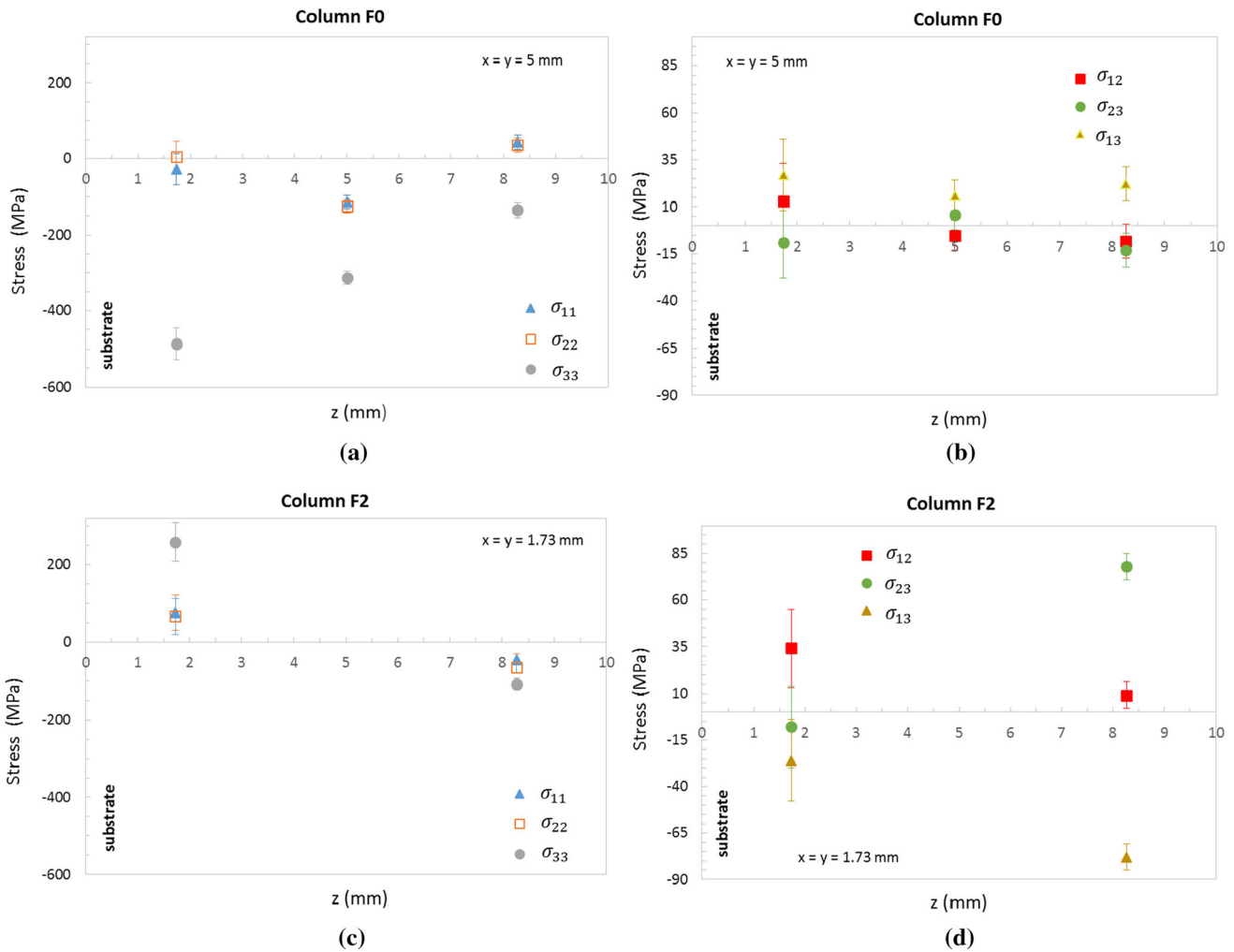
Fig. 3—Residual stresses obtained by ND at several building heights in the central column F0, *i.e.*, core sample (*a* and *b*) and the column F2 (*c* and *d*) close to a corner of the analyzed cube.

The mechanical properties of the specimen at ambient temperature have been characterized by monotonic tensile tests: $R_E = 985 \pm 12$ MPa (yield strength) and $\sigma_{UTS} = 1098 \pm 16$ MPa (ultimate tensile strength). In our study, stress magnitude is smaller than the yield strength of the samples close to the baseplate in agreement with.[34] The stress component $\sigma_{33} = -487 \pm 41$ MPa (column F0, $x = y = 5$ mm) gains on 50 pct of the yield strength.

Figure 3(b) illustrates the distributions of shear stress components (σ_{13}, σ_{23}, σ_{12}) in the central column F0. The shear stresses vary from -13 ± 9 MPa to 27 ± 19 MPa along the building direction.

In the column F2 ($x = y = 1.73$ mm), near a corner of the cube, the residual stress state is quite different from the previous case, especially for the normal stress component σ_{33} (Figure 3(c)). The stress magnitudes are lower due to the influence of the larger free surface with values ranging from $\sigma_{33} = 259 \pm 50$ MPa ($z = 1.73$ mm) to $\sigma_{33} = -108 \pm 14$ MPa ($z = 8.27$ mm). The sample shows an in-plane equi-biaxial stress state no matter the analyzed height. Longitudinal and transversal stress values are ranging from 76 ± 46 MPa to $-66 \pm$ 14 MPa (Figure 3(c)). As can be seen, tensile stresses develop at low z values (near the baseplate) while stresses turn into compression (slightly) with increasing z values. The highest shear stress values are obtained in the column F2 (Figure 3(d)) with values varying between 78 ± 7 MPa and -78 ± 7 MPa. In summary, the stress distribution near the surfaces tends to have a lower compressive magnitude, even reaching tension mechanical stress state, especially close to the baseplate at the cube corners (Figures 3(c) 4(a)). This is in agreement with previous works which showed that the bottom and top surfaces of LPBF specimens tend to be in tension or low compression while the internal volume of the part being in compression.[9,36]

C. The Effect of Assuming the Principal Directions in ND Measurements for Stress Analysis

As mentioned in the introductory chapter, in most previous studies, one strong assumption is usually made in order to reduce the number of measurement directions and thus the experiment duration (related to the low acquisition rate of ND technique). Latter entails
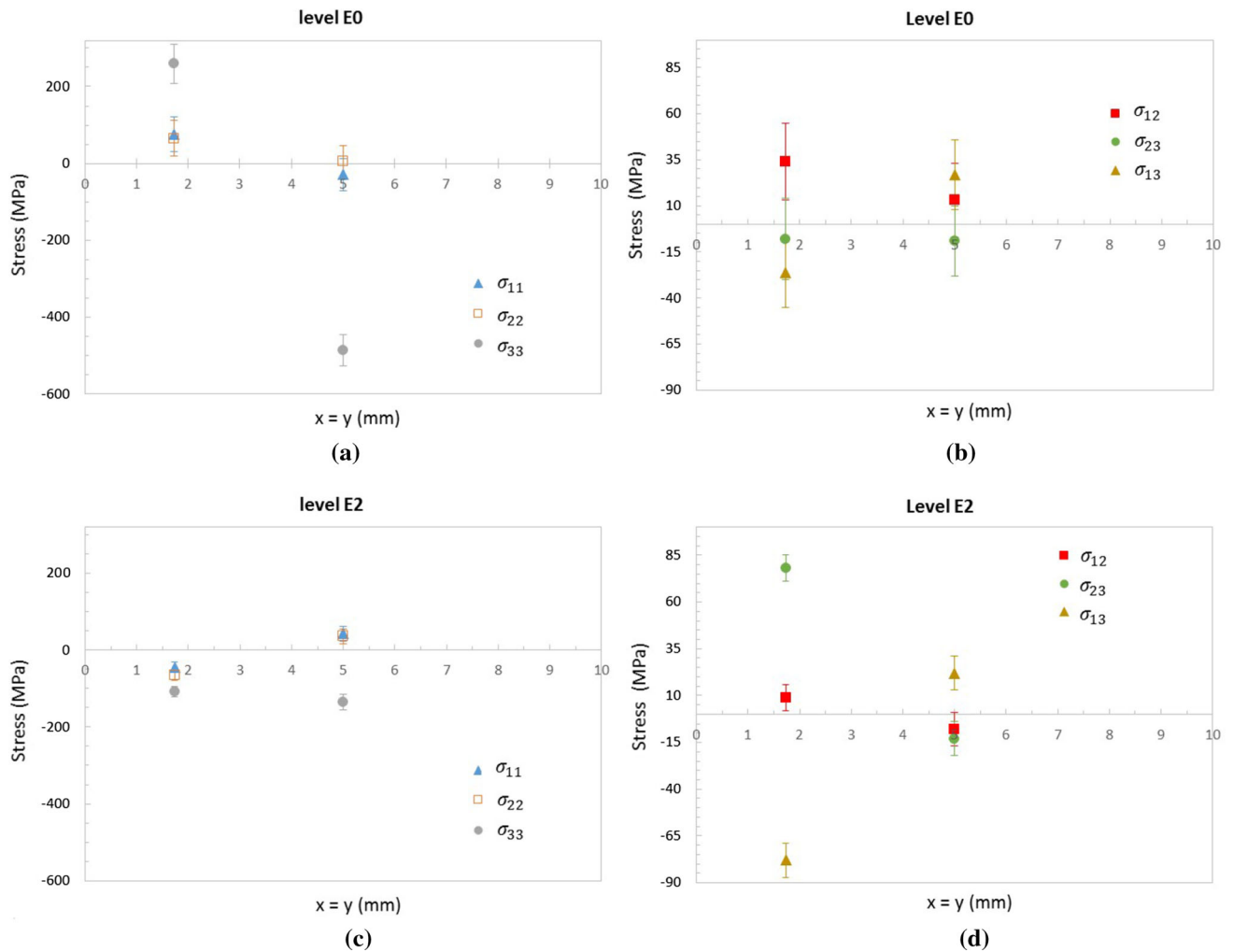
Fig. 4—Residual stresses obtained by ND at several building levels: close substrate (E1: *a* and *b*) and close surface (E2: *c* and *d*).

assuming that the principal stress coordinate system is known and can be inferred from the sample geometry. Strains can consequently be measured in only these 3 (orthogonal) directions to determine the principal stresses σ_1, σ_2, σ_3. This stress state assumption is not a true representation of the stress within the part, meaning that the use of Eqs. [5] or [6] may not provide the correct stress values. To highlight this problem, Table I shows the evolution of the principal stress components σ_i, calculated from the Eq. [5], compared to the results obtained for the normal components σ_{ii} with the relation [4] for the column F2. The 3 principal stress components σ_i have been determined from the Eq. [5] with the experimental lattice strain values measured at (φ, ψ) equal to (0, 0 deg), (0, 90 deg), and (90, 90 deg) for either each {hk.l} reflection or combining the three reflections simultaneously. For the second principal stress calculation method (reflection combination), since lattice strains were determined in three different sample directions per diffraction peak, we obtain 9 linear equations with three unknowns to which we applied a least-squares procedure to determine the best possible values for the three (unknown) principal stress

components σ_i. Finally, it should be underlined that there is no way to estimate the errors for the principal stress components when only 3 directions are used in stress analysis for a single reflection.

The principal stress values calculated with the relation [5] are different from the previous case (full stress tensor). The largest discrepancy is observed at $z = 1.73$ mm (E0F2). For example, the normal stress value along the *x*-direction (Figure 1) varies in a significant way according to the reflection selected in the stress analysis: $\sigma_1\{10.3\} = 202$ MPa, $\sigma_1\{11.2\} = 27$ MPa and $\sigma_1\{20.1\} = -291$ MPa. These results are quite different from those obtained previously with Eq. [4]: $\sigma_{11} = 76 \pm 46$ MPa. The largest difference is observed for the {20.1} reflection. This discordance could be partly attributed to the poor quality of the diffraction peaks for this reflection as regard to the low peak-to-background ratio (see Figure 2). The same trend is observed for the other diagonal tensor component values σ_2 and σ_3. However, at $z = 8.27$ mm (E2F2), the calculated σ_i values are close to the σ_{ii} values determined for the full stress tensor regardless the reflection or their combination.

Table I. Evolution of the Principal Stress Components σ_i, Calculated from Eq. [5], for Different {hk.l} Reflections and Compared to the Results Obtained for the Normal Components σ_{ii}, Obtained with the Relation [4], Along the Column F2

Stress Component	Assumption	E0F2	E2F2
σ_1 (MPa)	principal stress $-$ {10.3}	202	$-$ 46
	principal stress $-$ {11.2}	27	$-$ 37
	principal stress $-$ {20.1}	$-$ 291	$-$ 69
	principal stress {10.3} + {21.1} + {20.1}	$-$ 16 $\pm$ 135	$-$ 51 $\pm$ 16
	σ_{11}-full stress tensor	76 $\pm$ 46	$-$ 45 $\pm$ 14
σ_2 (MPa)	principal stress $-$ {10.3}	166	$-$ 74
	principal stress $-$ {11.2}	18	$-$ 51
	principal stress $-$ {20.1}	$-$ 277	$-$ 91
	principal stress {10.3} + {21.1} + {20.1}	$-$ 25 $\pm$ 135	$-$ 72 $\pm$16
	σ_{22}-full stress tensor	66 $\pm$ 46	$-$ 66 $\pm$ 14
σ_3 (MPa)	principal stress $-$ {10.3}	376	$-$ 137
	principal stress$-$ {11.2}	166	$-$ 84
	principal stress $-$ {20.1}	$-$ 354	$-$ 112
	principal stress {10.3} + {21.1} + {20.1}	62 $\pm$ 135	$-$ 110 $\pm$ 16
	σ_{33}-full stress tensor	259 $\pm$ 50	$-$ 108 $\pm$ 14

At this point, the difference between the normal stress, determined from Eq. [4], and the principal stress, obtained by Eq. [5], must be explained.[37,38] From the Eq. [4] which permits to calculate the full stress tensor, one can easily notice that the relation shows no coupling between both shear and normal stresses and strains as soon as three orthogonal lattice strains along the macroscopic coordinate axes are measured (*i.e.*, (φ, ψ) equal to (0, 0 deg), (0, 90 deg) and (90, 90 deg)):

$$\langle\varepsilon(hk.l, 0, 90)\rangle_{V_d} = \varepsilon_{11}$$
$$= \frac{1}{2} S_2(hk.l)\sigma_{11} + S_1(hk.l)[\sigma_{11} + \sigma_{22} + \sigma_{33}] \quad [7]$$

$$\langle\varepsilon(hk.l, 90, 90)\rangle_{V_d} = \varepsilon_{22}$$
$$= \frac{1}{2} S_2(hk.l)\sigma_{22} + S_1(hk.l)[\sigma_{11} + \sigma_{22} + \sigma_{33}] \quad [8]$$

$$\langle\varepsilon(hk.l, 0, 0)\rangle_{V_d} = \varepsilon_{33}$$
$$= \frac{1}{2} S_2(hk.l)\sigma_{33} + S_1(hk.l)[\sigma_{11} + \sigma_{22} + \sigma_{33}] \quad [9]$$

If the sample geometry coordinate system coincides with the principal stress coordinate system, the shear strain components are equal to 0 and the principal strains ε_i correspond to normal strains ε_{ii}. The principal strains ε_i can be determined by measuring lattice strains along the macroscopic coordinate axes and the principal stresses are calculated using Eqs. [7] through [9].

If the shear stress components have non-zero values, the principal stresses are not defined along the 3 sample coordinate axes but they are in other directions depending on the shear strain values. The assumption claiming that the sample geometry coordinate system does overlay the principle stress coordinate system is then wrong. The principal stresses may, therefore, be much larger depending on the magnitude of the shear strains. Since the normal stress components σ_{ii} do not depend on the values of the shear strains (Eqs. [7] through [9]), the stress components σ_{11}, σ_{22}, and σ_{33} are always true but not necessarily equal to the principal stresses σ_1, σ_2, and σ_3. In other words, the normal stress components in any three orthogonal directions may be correctly calculated by measuring the strains in these three directions whether or not they are the principal directions. This is always verified because the shear stress components do not affect the normal strains in a macroscopic isotropic material.[38]

Through the diagonalization of the full stress tensor,[37] it is possible to determinate the deviation of the principal stress directions (denoted (X, Y, Z)) from the LPBF part orthogonal axes (x, y, z) (defined in Figure 1) for each measurement point. Table II illustrates the angles between the principal stress directions and the specimen orthogonal stress directions.

In the central column, for the E0F0 and E1F0 measurements positions, the principal directions were aligned with the sample axes within approximately 20 degrees. The principal stress values were within $\pm$ 4 MPa of the corresponding orthogonal stress values shown in Figure 3(a). Near a corner of the cube (E0F2 and E2F2) or close to the top surface (E2F0), a large deviation is observed. This phenomenon is probably due to the influence of the free surface with a different thermal history of the probed region as compared to the internal volume of the part. The principal stress values are quite different from the normal stress component values. For example, at z = 8.27 mm (E2F2), the principal stress values (respectively the normal stress values) are: σ_1 = 27 MPa (σ_{11} = $-$ 45 MPa), σ_2 = $-$ 47 MPa (σ_{22} = $-$ 66 MPa), σ_3 = $-$ 199 MPa (σ_{33} = $-$ 108 MPa).

Table II. Angles Between the Principal Stress Directions (X, Y, Z) and the Specimen Orthogonal Stress Directions (x, y, z) for the Different Measurement Positions

Measurement Position	Angle between x And X (in Degree)	Angle Between y and Y (in Degree)	Angle Between z and Z (in Degree)
E0F0	19	19	4
E0F2	137	41	9
E1F0	19	18	5
E2F0	34	33	8
E2F2	51	42	40

Another problem arises when only three directions are used in stress analysis, there is no way to estimate the errors for the stress components. It is better to use a least-squares solution of Eq. [5] (respectively [4] for full stress tensor) which can be obtained when more than three (respectively six for full stress tensor) lattice strain measurements are performed. For example, at $z = 1.73$ mm (E0F2), although the {10.3} diffraction peaks are extremely well defined and thus their location accurately established, the relative difference of the principal components varies from 45 to 165 pct with the normal component values of the full stress tensor (Table I). When the three reflections are simultaneously taken into account (resolving 9 measurement directions instead of three), the large uncertainties given by the least-squares method allow for the solving quality of the equation system to be appraised (Table I) and enable thus the detection of anomalies in the stress analysis. At $z = 8.27$ mm (E2F2, Table I), the situation is in stark contrast to the previous one, with a low uncertainty. This allows us to conclude that the stresses, calculated by fitting the experimental data to Eq. [5], are a relevant analysis of the true state of strain/stress. It should be recalled that the calculated stress values obtained with Eq. [4] ($\sigma_1 = 51$ MPa, $\sigma_2 = -72$ MPa, $\sigma_3 = -110$ MPa) are close to the normal stress components determined by Eq. [5]. As explained above, the true principal stress values are different ($\sigma_1 = 27$ MPa, $\sigma_2 = -47$ MPa, $\sigma_3 = -199$ MPa) because a large deviation of the principal stress directions from the sample axes is observed (Table II).

D. Influence of Second-Order Stresses on Residual Stress Analysis in LPBF Produced Ti-6Al-4V Part

The full stress tensor has been determined with the relation [4] where the second-order stresses (or intergranular stresses) are neglected. In this case, the deviations of grain (mesoscopic) stresses from macroscopic stresses are hence considered to be solely due to elastic anisotropy. Residual stresses are also generated by inhomogeneous thermo-elastic or plastic deformations on two scales: one length scale is given by the size of the studied sample; the size of the grains forming the polycrystal defines the second one. The first-order (or macroscopic) stresses are given by the inhomogeneity on the part length scale. The second-order (or intergranular) stresses are given by the inhomogeneity on the grain size scale (mesoscopic scale). Both are superimposed and

a combination of first- and second-order stresses is given by ND measurements. Concerning the LPBF process, three origins of residual stresses can stand: difference in plastic flow caused by undergone stress, phase transformation or non-uniform shrinkage during cooling. If we have a superposition of both macroscopic and important intergranular contributions, the presence of intergranular strain influences the measured elastic strain. The stress values calculated by Eq. [4] will then necessarily vary with the {hk.l} reflection.[30,39] In most studies, stress analysis by XRD or ND is only performed with a single reflection. The importance of second-order stresses can thus never be quantified or even identified. To ascertain this, the evolution of the residual stresses for each of the 3 analyzed plane famillies {10.3}, {20.1}, and {11.2} alone are shown in Figure 5, and compared with the results obtained previously when the 3 reflections are simultaneously used for the complete stress analysis. For the sake of clarity, only σ_{33} evolution is shown for the columns F0 (Figure 5(a)) and F2 (Figure 5(b)).

The stress values change strongly from one reflection to another. For example, for the central column F0 at $z = 8.27$ mm, $\sigma_{33}(hk.l)$ values reach -230 ± 31 MPa for {20.1} and -84 ± 24 MPa for {11.2}. On the other hand, at $z = 1.73$ mm, the stress values for the different reflections are similar, with values ranging from -475 ± 20 to -516 ± 70 MPa. An opposite trend is observed for the column F2: at $z = 1.73$ mm, σ_{33} values significantly differ ($\sigma_{33}(10.3) = 396 \pm 32$ MPa and $\sigma_{33}(11.2) = 144 \pm 30$ MPa) while, at $z = 8.27$ mm, closer stress values are determined by ND. It should be noted that this phenomenon is not due to a limited set of measurement directions (10 (φ, ψ) directions per reflection in the present case). The uncertainties obtained for each reflection are similar to those determined for the full stress tensor. The fitting of the data to Eq. [4] seems to be proper as revealed by the low level of the estimated uncertainties. The results obtained previously, when the three reflections are used simultaneously, logically show intermediate values (Figure 5). The calculated stress clearly depends on the analyzed plane family. This reflection dependence of the stress values obtained by ND clearly indicates that strain incompatibilities are present at the grain scale. The diffracting grains are not the same for each {hk.l} reflection and this allows us to deduce that different second-order stresses exist, related to a strong thermic and/or plastic anisotropic deformation for this set of grains. High-temperature gradients,
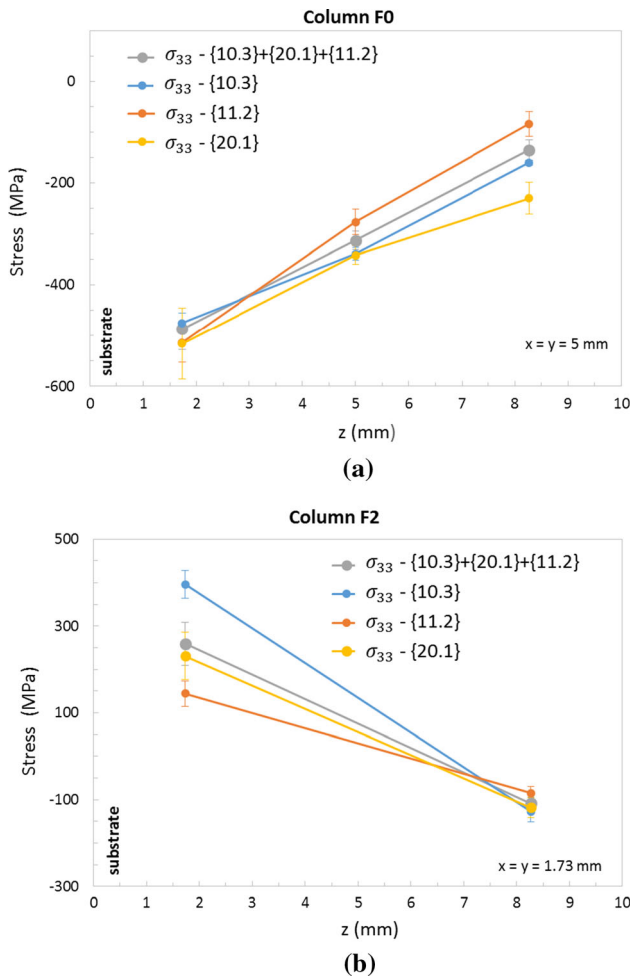
Fig. 5—Stress distribution determined with the relation [4] using a single (either {10.3} or {11.2} or {20.1}) or multiple ({10.3} + {11.2} + {20.1}) {hk.l} reflections for stress analysis along F0 (*a*) and F2 (*b*) columns.

as a result of the locally concentrated energy input, lead to high stress gradients. A residual stress gradient between core regions and the surface of the part is present. Its magnitude depends on the part geometry, the material stiffness and the temperature fields. As a consequence, the development of stress is locally affected and depends on the location in the sample. The development of second-order stresses is strongly dependent on the thermal history of the probed region. However, the results obtained with several {hk.l} reflections provide valuable information on the residual stress generation and should reduce the effects of second-order stresses on the macroscopic stress evaluation due to its averaging effect.

IV. CONCLUSIONS

In this present work, the residual stress distribution in a Ti-6Al-4V sample, produced by means of LPBF technology, has been evaluated using ND. Residual stress development in LPBF parts is mostly caused by

large cooling rates and high-temperature gradient, proper to the process. The bottom and top surfaces of LPBF specimens tend to be in tension or low compression while the internal volume stands in compression. Residual stress in the LPBF part could be reduced and homogenized through the optimization of process parameters (*e.g.*, pre-heating, scanning strategy). A relevant mapping of the stress values through the full depth of AM parts has to consider the full stress tensor consisting of six stress components, otherwise determined stress values might be distorted or even wrong, mistaking between compression and tension stress state. Furthermore, in LPBF process, non-negligible residual second-order stress gradients arise from the different interdependent physical phenomena (metallurgical, thermal, mechanical and fluid mechanic aspects) occurring during this highly non-equilibrium process for hexagonal alloys which are generally highly anisotropic materials. These stresses can be detected by ND with the use of multiple {hk.l} reflections. To obtain a relevant stress analysis, a large number of (φ, ψ) directions (*i.e.*, more than six lattice strain measurements) is required to minimize the effects of a single erroneous reflection profile measurement and to enable an assessment of the quality of the least-squares fitting to the experimental data.

REFERENCES

1. E. William Frazier: *J. Mater. Eng. Perform.*, 2014, vol. 23, pp. 1917–28.
2. C.Y. Yap, C.K. Chua, Z.L. Dong, Z.H. Liu, D.Q. Zhang, L.E. Loh, and S.L. Sing: *Appl. Phys. Rev.*, 2015, vol. 2, pp. 1–21.
3. L.-C. Zhang and H. Attar: *Adv. Eng. Mater.*, 2016, vol. 18, pp. 463–75.
4. W.S.W. Harun, N.S. Manam, M.S.I.N. Kamariah, S. Sharif, A.H. Zulkifly, I. Ahmad, and H. Miura: *Powder Technol.*, 2018, vol. 331, pp. 74–97.
5. J.-P. Kruth, L. Froyen, J. Van Vaerenbergh, P. Mercelis, M. Rombouts, and B. Lauwers: *J. Mater. Process. Technol.*, 2004, vol. 149, pp. 616–22.
6. D.W. Brown, J.D. Bernardin, J.S. Carpenter, B. Clausen, D. Spernjak, and J.M. Thompson: *Mater. Sci. Eng. A*, 2016, vol. 678, pp. 291–98.
7. M. Awd, J. Tenkamp, M. Hirtler, S. Siddique, M. Bambach, and F. Walther: *Materials*, 2018, vol. 11, pp. 1–17.

8. B. Vrancken: Study of residual stresses in selective laser melting, Faculty of engineering Science. PhD Dissertation, University of Leuven, 2016.
9. P. Mercelis and J.-P. Kruth: *Rapid Prototyp. J.*, 2006, vol. 12, pp. 254–65.
10. H. Shipley, D. McDonnell, M. Culleton, R. Coull, R. Lupoi, G. O'Donnell, and D. Trimble: *Int. J. Mach. Tool. Manu.*, 2018, vol. 128, pp. 1–20.
11. M.B. Prime: *J. Eng. Mater. Tech.*, 2000, vol. 123, pp. 162–68.
12. ASTM Standard E837 REV A: Standard Test Method for Determining Residual Stresses by the Hole-Drilling Strain-Gage Method, ASTM International, West Conshohocken, PA, 2013.
13. M.B. Prime: *Appl. Mech. Rev.*, 1999, vol. 52, pp. 75–96.
14. Y. Liu, Y. Yang, and D. Wang: *Int. J. Adv. Manuf. Tech.*, 2016, vol. 87, pp. 647–56.
15. L.S. Anderson, A.M. Venter, B. Vrancken, D. Marais, J. Van Humbeeck, and T.H. Becker: *Mater. Res. Proc.*, 2018, vol. 4, pp. 73–78.
16. V. Hauk: *Structural and Residual Stress Analysis by Nondestructive Methods*, Elsevier, Amsterdam, 1997.
17. D. Gloaguen, G. Oum, V. Legrand, J. Fajoui, and S. Branchu: *Acta Mater.*, 2013, vol. 61, pp. 5779–90.
18. L. Pintschovius, V. Jung, E. Macherauch, and O. Vohringer: *Mater. Sci. Eng.*, 1983, vol. 61, pp. 43–50.
19. L. Steven Anderson: Evaluating measurement techniques: establishing a testing framework for residual stress in selective laser melted Ti-6Al-4V, Faculty of Engineering PhD Dissertation, University of Stellenbosch, 2017.
20. A. Kromm, S. Cabeza, T. Mishurova, N. Nadammal, T. Thiede, and G. Bruno: *Mater. Res. Proc.*, 2018, vol. 6, pp. 259–64.
21. V.-D. Le, E. Pessard, F. Morel, and F. Edy: *Eng. Fract. Mech.*, 2019, vol. 214, pp. 410–26.
22. B.B. He: *Two-Dimensional X-ray Diffraction*, Wiley, Hoboken, 2018, pp. 292–93.
23. P.J. Withers, M. Preuss, A. Steuwer, and J.W.L. Pang: *J. Appl. Cryst.*, 2007, vol. 40, pp. 891–904.
24. H. Dölle and V. Hauk: *Z. Metalkde*, 1978, vol. 69, pp. 410–17.
25. A. Baczmanski, N. Hfaiedh, M. François, and K. Wierzbanowski: *Mater. Sci. Eng. A*, 2009, vol. 501, pp. 153–65.
26. I.C. Noyan: *Mater. Sci. Eng.*, 1985, vol. 75, pp. 95–103.
27. M. Hofmann, W. Gan, and J. Rebelo-Kornmeier: *J. Large-Scale Res. Facil.*, 2015, vol. 1A6, pp. 1–4.
28. J. Rebelo Kornmeier, M. Hofmann, W.M. Gan, C. Randau, K. Braun, K. Zeitelhack, I. Defendi, J. Krueger, E. Faulhaber, and H. Brokmeier: *Mater. Sci. Forum*, 2017, vol. 905, pp. 151–56.
29. G. Simmons and H. Wang: *Single Crystal Elastic Constants and Calculated Aggregate Properties*, MIT Press, Cambridge, 1971.
30. D. Gloaguen, T. Berchi, E. Girard, and R. Guillén: *J. Nucl. Mater.*, 2008, vol. 374, pp. 138–46.
31. U.F. Kocks, C.N. Tomé, and H.R. Wenk: *Texture and Anisotropy*, Cambridge University Press, Cambridge, 1998, pp. 288–89.
32. T. Simson, A. Emmel, A. Dwars, and J. Böhm: *Addit. Manuf.*, 2017, vol. 17, pp. 183–89.
33. C. Li, Z.Y. Liu, X.Y. Fang, and Y.B. Guo: *Procedia CIRP*, 2018, vol. 71, pp. 348–53.
34. H. Ali, L. Ma, H. Ghadbeigi, and K. Mumtaz: *Mater. Sci. Eng. A*, 2017, vol. 695, pp. 211–20.
35. R. Mertens, B. Vranchen, N. Holmstock, Y. Kinds, J.-P. Kruth, and J. Van Humbeeck: *Phys. Proc.*, 2016, vol. 83, pp. 882–90.
36. I. Yadroitec and I. Yadroitsava: *Virtual Phys. Prototyp.*, 2015, vol. 10, pp. 67–76.
37. M.E. Fitzpatrick and A. Lodini: *Analysis of Residual Stress by Diffraction using Neutron and Synchrotron radiation*, Taylor & Francis, Routledge, 2003.
38. R.A. Winholtz and A.D. Krawitz: *Mater. Sci. Eng. A*, 1996, vol. 205, pp. 257–58.
39. D. Gloaguen, M. François, and R. Guillén: *J. Appl. Cryst.*, 2004, vol. 37, pp. 934–40.